High-Performance Visible-Light-Driven SnS$_2$/SnO$_2$ Nanocomposite Photocatalyst Prepared via In situ Hydrothermal Oxidation of SnS$_2$ Nanoparticles

Yong Cai Zhang,*,[†] Zhen Ni Du,[†] Kun Wei Li,[‡] Ming Zhang,[†] and Dionysios D. Dionysiou[§]

[†]Key Laboratory of Environmental Material and Environmental Engineering of Jiangsu Province, College of Chemistry and Chemical Engineering, Yangzhou University, Yangzhou 225002, China

[‡]Food and Agriculture Standardization Institute, China National Institute of Standardization, 4 Zhichun Road, Haidian District, Beijing 100088, China

[§]Department of Civil and Science Program, University of Cincinnati, Cincinnati, Ohio 45221-0012, United States

Ⓢ *Supporting Information*

ABSTRACT: SnS$_2$/SnO$_2$ nanocomposites with tunable SnO$_2$ contents were prepared via in situ hydrothermal oxidation of SnS$_2$ nanoparticles in 0.375−4.5 mass% H$_2$O$_2$ aqueous solutions at 180 °C for 0−12 h. The structure, composition and optical properties of the as-prepared SnS$_2$/SnO$_2$ nanocomposites were characterized by X-ray diffraction, transmission electron microscopy, high-resolution transmission electron microscopy, Brunauer−Emmett−Teller (BET) surface area analysis, energy-dispersive X-ray spectroscopy, X-ray photoelectron spectroscopy, and UV−vis diffuse reflectance spectra.

Furthermore, their photocatalytic properties were tested for the degradation of methyl orange in water under visible light ($\lambda > 420$ nm) irradiation. It was found that the as-prepared SnS$_2$/SnO$_2$ nanocomposites with suitable SnO$_2$ content not only demonstrated superior photocatalytic activity to both SnS$_2$ nanoparticles and physically mixed SnS$_2$/SnO$_2$ composite nanoparticles, but also had remarkable photocatalytic stability. The tight attachment of SnO$_2$ nanoparticles to SnS$_2$ nanoparticles, which can facilitate interfacial electron transfer and reduce the self-agglomeration of two components, was considered to play an important role in achieving the high photocatalytic performances exhibited by the as-prepared SnS$_2$/SnO$_2$ nanocomposites.

KEYWORDS: tin sulfide, tin oxide, nanocomposites, in situ oxidation synthesis, photocatalysis, stability
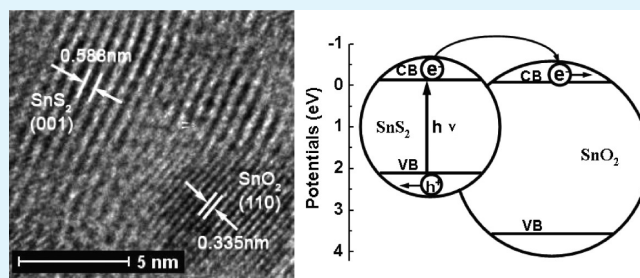
1. INTRODUCTION

Nowadays, there is an increasing interest in the application of semiconductors as photocatalysts to degrade organic pollutants, which are hazardous to human health, harmful to the environment, and difficult to degrade by natural means. TiO$_2$ is undoubtedly the most studied semiconductor photocatalyst by far, in view of its low cost, high activity for many photocatalytic reactions, chemical and photochemical stability, and biocompatibility.[1−3] However, it can absorb only ultraviolet light because of its wide band gap (3.2 eV),[1−3] and is not responsive to visible light ($\lambda > 400$ nm), which accounts for around 46% of the total solar energy.[4] To make full use of solar energy, it is desirable to exploit novel visible light-sensitive semiconductor photocatalysts.

The semiconducting metal sulfides usually have light-absorbing ability in the visible and short-wavelength near-infrared regions, which enable them to work as a promising class of visible light-driven photocatalysts[5−9] or sensitizers for wide band gap semiconductors.[10−20] Among them, CdS with a band gap of about 2.4 eV, is currently the focus of significant attention.[5−7] However, CdS itself is detrimental to human health and the environment due to its high toxicity. Tin disulfide (SnS$_2$) is a

CdI$_2$-tpye layered semiconductor with a band gap of about 2.2−2.35 eV,[9,10] which is a little smaller than that of CdS. SnS$_2$ is nonpoisonous, relatively inexpensive, chemically stable in acid or neutral aqueous solution, and thus it has the potential to be a good visible light-sensitive photocatalyst.[9−11] Although SnS$_2$ has unique advantages such as relatively low toxicity and wider spectrum response (or higher activity) as compared with CdS, only a few reports on its photocatalytic performance are available to date.[8−11] Therefore, from the viewpoints of both fundamental science and practical applications, more research should be pursued to explore the properties of SnS$_2$-based photocatalysts.

In comparison to single semiconductor, the coupling between two different semiconductors has proved to be successful in developing higher performance photocatalysts.[10−30] The improved photocatalytic activity of composite semiconductors is attributed to a large extent to the enhanced separation of photoinduced electrons and holes via interfacial charge transfer.[10−30]

Table 1. Abbreviated Names and Properties of the Products Prepared via In situ Hydrothermal Oxidation of SnS$_2$ Nanoparticles under Different Conditions, Together with the Properties of the Starting SnS$_2$ Nanoparticles

names	H$_2$O$_2$ (mass%)	t (h)	SnO$_2$ mass%	size (nm)	BET surface area (m^2/g)	E_g (eV)
SnS$_2$			0	9—18	104.5	2.25
SnS$_2$/SnO$_2$-(a)	0.375	0	18.1	9—18	87.3	2.31
SnS$_2$/SnO$_2$-(b)	0.375	6	22.5	11—23	83.8	2.33
SnS$_2$/SnO$_2$-(c)	0.375	12	24.6	12—26	64.4	2.31
SnS$_2$/SnO$_2$-(d)	3.0	12	81.0	4—32	53.1	2.31
SnO$_2$	4.5	12	100	4—8	148.1	3.66

Thus, the interface between coupled semiconductors which serves as the site of the transfer and subsequent trapping of photogenerated charge carriers is quite important.[10−30]

One common method to fabricate composite photocatalysts is the simple physical mixing of two different semiconductors (SC1 and SC2) with matched band potentials. However, the particles of SC1 and SC2 in such kind of composites are not tightly attached to each other and inclined to separate and self-agglomerate when dispersed in the solution. The interface arises only when the particles of SC1 and SC2 collide. As a result, the probability of charge carrier separation at the momentary interface induced by random collision of separated SC1 and SC2 particles is rather low. Compared with the physical mixing method, the in situ chemical synthesis is capable of forming more homogeneous mixture and stronger interaction between SC1 and SC2 particles with a tighter interface, which helps the interfacial charge transfer and reduces the self-agglomeration of the two components. Accordingly, the photocatalytic performances of the composite semiconductors synthesized via in situ chemical methods often surpass those prepared via physical mixing methods.[10,27−30]

SnO$_2$ is a stable oxide semiconductor with a wide band gap of about 3.5−3.6 eV.[31,32] Its choice as a coupling semiconductor to SnS$_2$ has at least two distinct advantages. First, SnO$_2$ and SnS$_2$ have matched band potentials (both the valence band (VB) and conduction band (CB) potentials of SnS$_2$ are more negative (or energetically higher) than those of SnO$_2$). This allows the photoinduced electron transfer from the CB of SnS$_2$ to the CB of SnO$_2$, which can enhance the separation of photogenerated charge carriers and bring about the sensitization of SnO$_2$.[33] So, it is reasonable to expect that the photocatalytic efficiency of SnS$_2$/SnO$_2$ nanocomposites would be higher than that of individual SnS$_2$ nanoparticles. Second, the synthesis of SnS$_2$/SnO$_2$ nanocomposites with tunable and uniform composition as well as tighter interface can be easily realized, for instance, via in situ oxidization of SnS$_2$ nanoparticles by H$_2$O$_2$ under hydrothermal conditions, as will be shown below in this study.

Herein, we report an alternative simple and cost-effective synthesis of SnS$_2$/SnO$_2$ nanocomposites via in situ oxidation of SnS$_2$ nanoparticles by H$_2$O$_2$ under hydrothermal conditions. The photocatalytic properties of the resultant SnS$_2$/SnO$_2$ nanocomposites are evaluated for the degradation of methyl orange (MO) in water under visible light ($\lambda > 420$ nm) irradiation, and compared with those of SnS$_2$ nanoparticles and physically mixed SnS$_2$/SnO$_2$ composite nanoparticles. To the best of our knowledge, this is the first report on the photocatalytic properties of SnS$_2$/SnO$_2$ composite semiconductors so far.

2. EXPERIMENTAL SECTION

All the chemical reagents used were of analytical grade and purchased directly from Sinopharm Chemical Reagent Co., Ltd. SnS$_2$ nanoparticles

were synthesized through hydrothermal reaction between 5 mmol SnCl$_4$·5H$_2$O and 10 mmol of thioacetamide in 5 vol % acetic acid aqueous solution at 120 °C for 12 h.

2.1. Synthesis of SnS$_2$/SnO$_2$ nanocomposites. 0.4 g of SnS$_2$ nanoparticles was weighed into a Teflon-lined stainless steel autoclave of 50 mL capacity, then 40 mL of 0.375−4.5 mass% H$_2$O$_2$ aqueous solution was added in with stirring. The autoclaves were sealed and heated in an electric oven at 180 °C for 0−12 h (t = 0 h, that is, the electric oven was powered off immediately once the temperature rose from room temperature to 180 °C), and then allowed to cool to room temperature naturally. The resulting yellowish or white precipitates were filtered, washed with deionized water and ethanol, and dried in a vacuum at 100 °C.

For the convenience of description, the SnS$_2$/SnO$_2$ nanocomposites obtained under different conditions were hereinafter called as "SnS$_2$/SnO$_2$-(a)", "SnS$_2$/SnO$_2$-(b)", and "SnS$_2$/SnO$_2$-(c)", etc., as shown in Table 1.

2.2. Characterization. X-ray diffraction (XRD) patterns of the products were measured on a German Bruker AXS D8 ADVANCE X-ray diffractometer at a scanning speed of 1.2°/min. EDX spectra were taken on a Japan Hitachi S-4800 field emission scanning electron microscopy. X-ray photoelectron spectroscopy (XPS) measurements were performed on an American Thermo-VG Scientific ESCALAB 250 XPS system with Al K$_\alpha$ radiation as the exciting source, where the binding energies were calibrated by referencing the C 1s peak (284.6 eV) to reduce the sample charge effect. Transmission electron microscopy (TEM) images were taken on a Holland Philips Tecnai−12 transmission electron microscopy. High-resolution transmission electron microscopy (HRTEM) images were taken on an American FEI Tecnai G2 F30 S-TWIN field-emission transmission electron microscopy. BET surface areas were measured on an American Micromeritics Instrument Corporation TriStar II 3020 surface area and porosity analyzer. UV−vis diffuse reflectance spectra were obtained on a Japan Shimadzu UV-3101PC ultraviolet−visible-near-infrared spectrophotometer, using BaSO$_4$ as a reference.

2.3. Photocatalytic Tests. Photocatalytic properties of the as-prepared products were studied by degrading aqueous MO under visible light ($\lambda > 420$ nm) irradiation. For comparison, the physically mixed SnS$_2$/SnO$_2$ composite containing 81.9 mass % SnS$_2$ nanoparticles and 18.1 mass % SnO$_2$ nanoparticles, which is later called as PM-SnS$_2$/SnO$_2$, was also tested under the same conditions.

The photocatalytic experiments were conducted in a homemade photochemical reactor [9], which includes mainly four parts: light source system including an 1000 W Xe lamp, ($\lambda > 420$ nm) cutoff filters and cooling attachments such as air pump and electric fan; reactor (two-layer Pyrex glass bottles of 400 mL capacity, the space between the two layers is filled with circulating water to cool the reactor); magnetic stirrer; and temperature controller. In each experiment, the distance between the Xe lamp and the reactor was set to be 10 cm, and the reaction temperature was 25 °C. Prior to illumination, 300 mL of MO aqueous solutions containing different samples were magnetically stirred in the dark for 1 h to achieve adsorption/desorption equilibrium
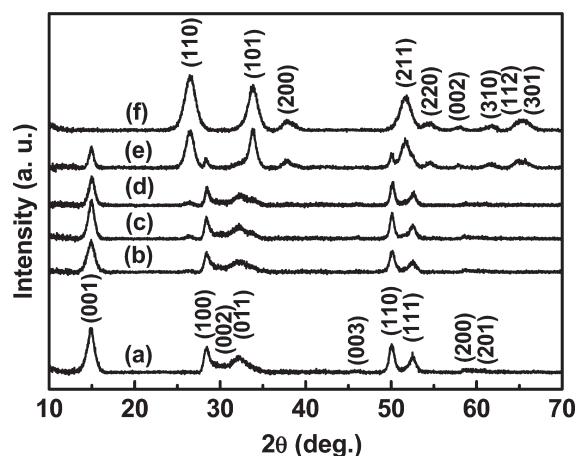
Figure 1. XRD patterns of the as-prepared (a) SnS_2, (b) SnS_2/SnO_2-(a), (c) SnS_2/SnO_2-(b), (d) SnS_2/SnO_2-(c), (e) SnS_2/SnO_2-(d), and (f) SnO_2.

between the photocatalysts and MO. During illumination, about 4.0 mL of suspension was taken from the reactor at an interval of 10 min and centrifugated to separate the photocatalyst. The supernatant solution was analyzed by a Japan Shimadzu UV-2550 UV—vis spectrophotometer at the maximum absorption wavelength of MO (462.0 nm).

3. RESULTS AND DISCUSSION

3.1. Structural and Composition Characterization. Figure 1a shows the XRD pattern of SnS_2 nanoparticles, while Figure 1b—f show the XRD patterns of the products prepared via in situ hydrothermal oxidation of SnS_2 nanoparticles in different concentrations of H_2O_2 aqueous solutions at 180 °C for 0—12 h. Although XRD peaks in a and f in Figure 1 can be indexed to pure hexagonal phase SnS_2 (JCPDS card no. 89—2358) and tetragonal phase SnO_2 (JCPDS card no. 41—1445), respectively, those in Figure 1b—e indicate the formation of SnS_2 and SnO_2 mixtures. The SnO_2 contents in the as-prepared SnS_2/SnO_2 composites were determined by EDX, and the analysis results are shown in Table 1. It can be seen from Table 1 that the relative contents of SnO_2 in the as-prepared composites can be adjusted from 18.1 to 81.0 mass % through varying the concentrations of H_2O_2 aqueous solution and the reaction times.

The as-prepared SnS_2/SnO_2-(a) was further characterized by XPS, whose results are shown in Figure 2. It can be seen from the Sn 3d spectra in Figure 2(a) that the binding energy (486.82 eV) of Sn 3d5/2 in SnS_2/SnO_2-(a) lies between those in SnS_2 (486.65 eV) and SnO_2 (486.90 eV). In addition, the binding energies of S 2p3/2 and O1s in SnS_2/SnO_2-(a) were observed at about 161.72 (Figure 2b) and 530.71 eV (Figure 2c), respectively, which also agreed with the reference values for SnS_2 and SnO_2 crystals.[34] Because the combination with S^{2-} or O^{2-} cannot cause obvious change in the binding energy of Sn^{4+},[34] it was hard to say whether there were chemical bonds existing between SnS_2 and SnO_2 in SnS_2/SnO_2-(a) simply from XPS characterization. But, the above XPS analysis results at least confirmed that SnS_2/SnO_2-(a) was indeed a composite of SnS_2 and SnO_2.
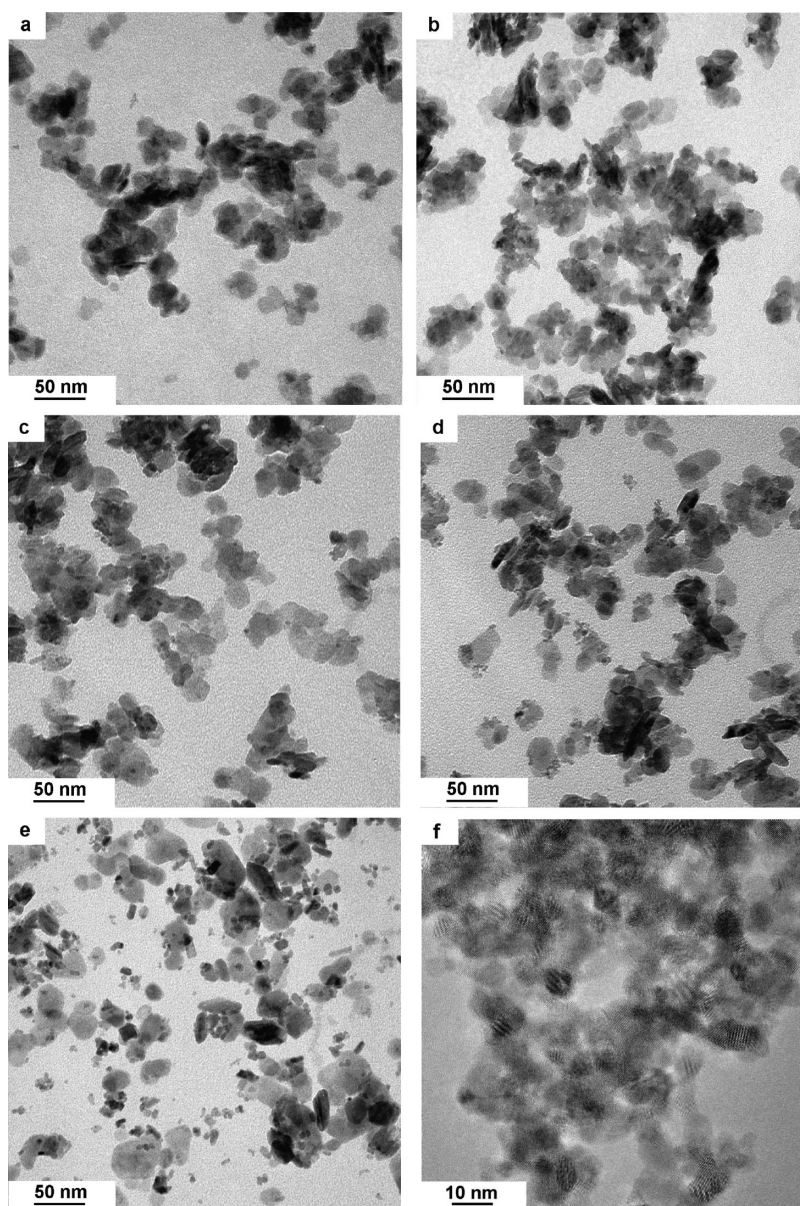
Figure 3a—f shows the TEM images of the as-prepared SnS_2, SnS_2/SnO_2-(a)—(d) and SnO_2. As can be seen, all the samples in Figure 3a—f consisted of nanoparticles, whose sizes are summarized in Table 1. Nevertheless, it seemed that SnS_2/SnO_2-(a) with
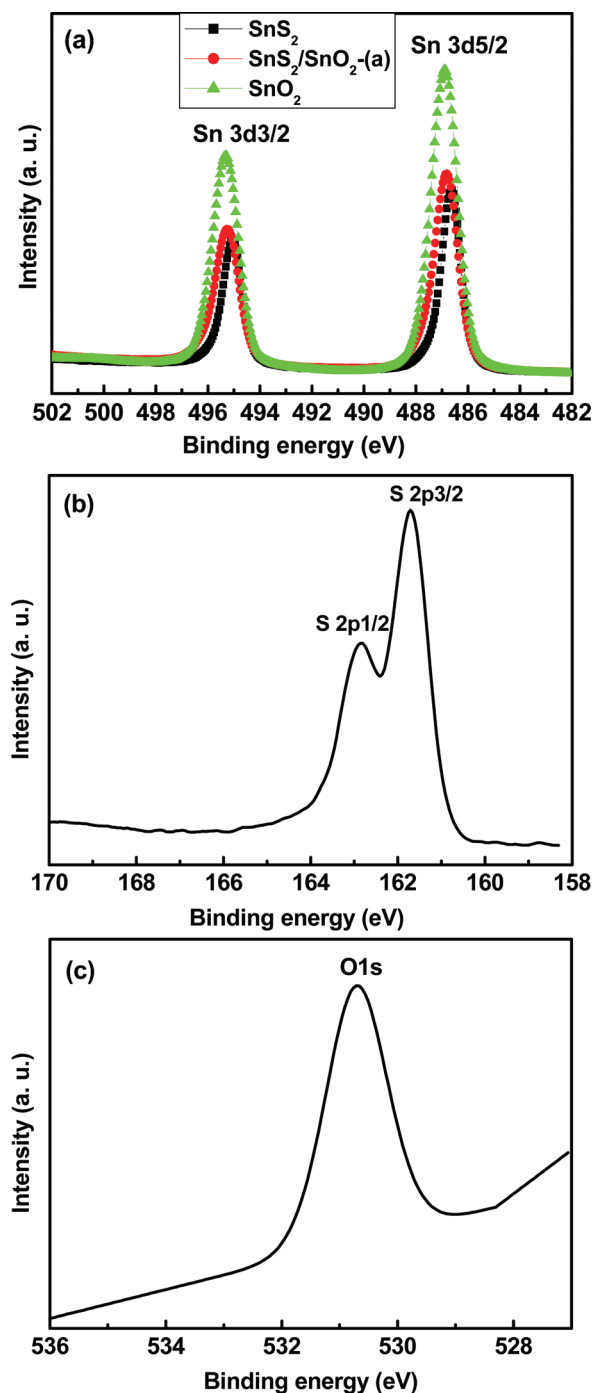
Figure 2. XPS spectra of (a) Sn 3d, (b) S 2p, and (c) O 1s in SnS_2/SnO_2-(a).

the lowest content of SnO_2 had particle size and size distribution similar to its precursor, SnS_2 nanoparticles, whereas SnS_2/SnO_2-(d) with the highest content of SnO_2 comprised distinctly nonuniform nanoparticles with a wide size distribution (further HRTEM characterization disclosed that the smallest (4—8 nm) nanoparticles in Figure 3e belonged to SnO_2). This was probably because moderate oxidation enabled the whole attachment of SnO_2 nanoparticles to SnS_2 nanoparticles, but too much oxidation caused the partial separation of these two kinds of nanoparticles, giving rise to many unattached SnO_2 nanoparticles.

1530

dx.doi.org/10.1021/am200102y |*ACS Appl. Mater. Interfaces* 2011, 3, 1528–1537

Figure 3. TEM images of the as-prepared (a) SnS_2, (b) SnS_2/SnO_2-(a), (c) SnS_2/SnO_2-(b), (d) SnS_2/SnO_2-(c), (e) SnS_2/SnO_2-(d), and (f) SnO_2.

The microstructure of SnS_2/SnO_2-(a) was further observed by means of HRTEM. As can be seen from HRTEM images a and b in Figure 4, the SnS_2/SnO_2-(a) nanoparticles displayed clear lattice fringes, suggesting their crystalline nature. The fringe interval of 0.588 nm was in agreement with the interplanar spacing of (001) crystal planes of hexagonal phase SnS_2, whereas that of 0.335 nm corresponded to the interplanar spacing of (110) crystal planes of tetragonal phase SnO_2. Moreover, smaller-sized SnO_2 nanoparticles were tightly attached to the surface of large-sized SnS_2 nanoparticles, and they can not be separated from each other even by continuous ultrasonic dispersion in water for one hour. The HRTEM images clearly revealed the formation of SnS_2/SnO_2 nanocomposite with a firm interface, which would make the interfacial electron transfer spatially available and smooth, and accordingly increase the photocatalytic activity.

As is well-known, SnS_2 belongs to hexagonal crystal system (S.G.: $P\bar{3}m1$ (164)) with the lattice constants of $a = b = 0.365$ nm

and $c = 0.589$ nm, whereas SnO_2 belongs to tetragonal crystal system (S.G.: $P4_2/mnm$ (136)) with the lattice constants of $a = 0.474$ nm and $c = 0.319$ nm. It can be observed from Figure 4b that the intersection angle between $(110)_{SnO2}$ and $(0001)_{SnS2}$ is about 17°. In SnO_2 crystal, the normal direction of $2\bar{1}0$ crystal plane was calculated to intersect with (110) crystal plane at an angle of 18.4°, closest to 17°. So, we considered that the lattice match occurred between $(2\bar{1}0)_{SnO2}$ and $(10\bar{1}0)_{SnS2}$, as shown in Figure 5a. From the two-dimensional lattice diagrams of $(2\bar{1}0)_{SnO2}$ (Figure 5b) and $(10\bar{1}0)_{SnS2}$ (Figure 5c), it can be seen that the lattice point spacings along $[120]_{SnO2}$, $[001]_{SnO2}$, $[0001]_{SnS2}$ and $[1\bar{2}10]_{SnS2}$ crystal orientations are in turn, 1.059, 0.319, 0.588, and 0.365 nm. Obviously, the lattice point spacing of $[120]_{SnO2}$ is nearly twice that of $[0001]_{SnS2}$, and the calculated lattice mismatch is 9.95%. In another matching direction (that is, $[001]_{SnO2}$ and $[1\bar{2}10]_{SnS2}$), the lattice mismatch was calculated to be 12.6%. Since the lattice mismatches are in the range of 5−25%, the semicoherent structure may be formed between
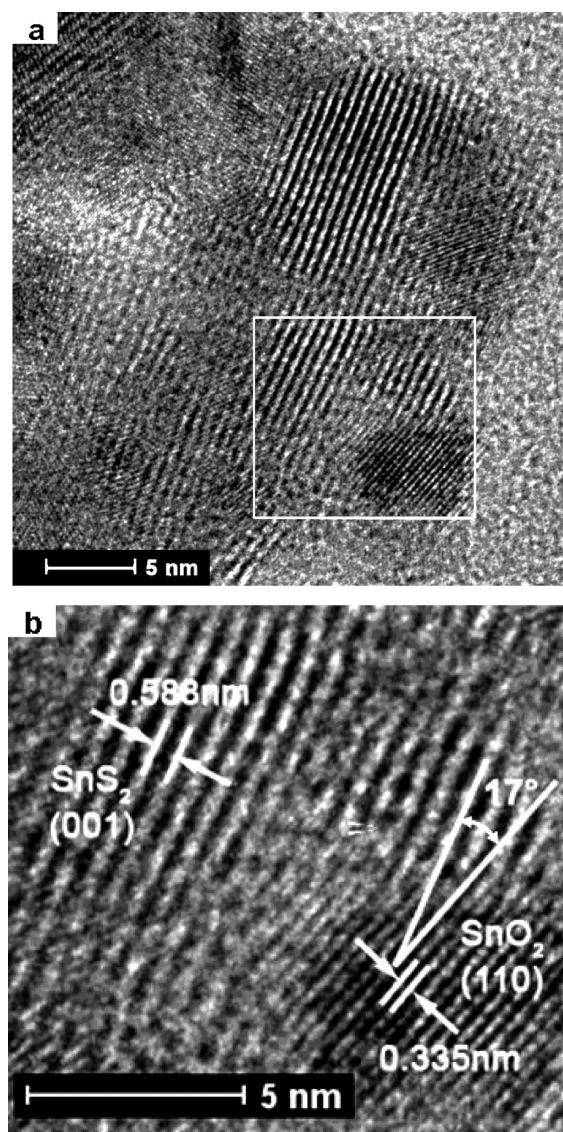
Figure 4. HRTEM images of SnS$_2$/SnO$_2$-(a).

Figure 5. (a) Lattice mismatch diagram between SnS$_2$ and SnO$_2$ in SnS$_2$/SnO$_2$-(a), and two-dimensional lattice diagrams of (b) $(2-10)_{SnO2}$ and (c) $(10-10)_{SnS2}$.

$(2\bar{1}0)_{SnO2}$ and $(10\bar{1}0)_{SnS2}$. The slight difference between the calculated (18.4°) and observed (17°) intersection angles is very likely attributed to the lattice mismatch, which can induce the lattice distortion and edge dislocation on both sizes of the interface.

3.2. Formation Mechanism. The formation mechanism of the SnS$_2$/SnO$_2$ nanocomposites with a contact interface, instead of a core–shell structure, may be interpreted as follows. First, hexagonal phase SnS$_2$ has an anisotropic CdI$_2$-tpye layered crystal structure,[35,36] whose different exposed crystal faces possess diverse reactive activity. In addition, a large amount of "broken" surface or dangling bonds and other surface defects intrinsically exist in the nanocrystalline materials.[37–39] It is common believed that the surface defects of crystal are more reactive sites.[37–39] Second, the very diluted H$_2$O$_2$ aqueous solutions (0.375–3.0 mass%) used in the synthesis of composite products have a weak oxidation ability, and may preferentially react with the more reactive exposed crystal faces or surface defect centers of SnS$_2$ nanoparticles. Third, the oxidation product SnO$_2$ tends to nucleate and grow on the reaction sites

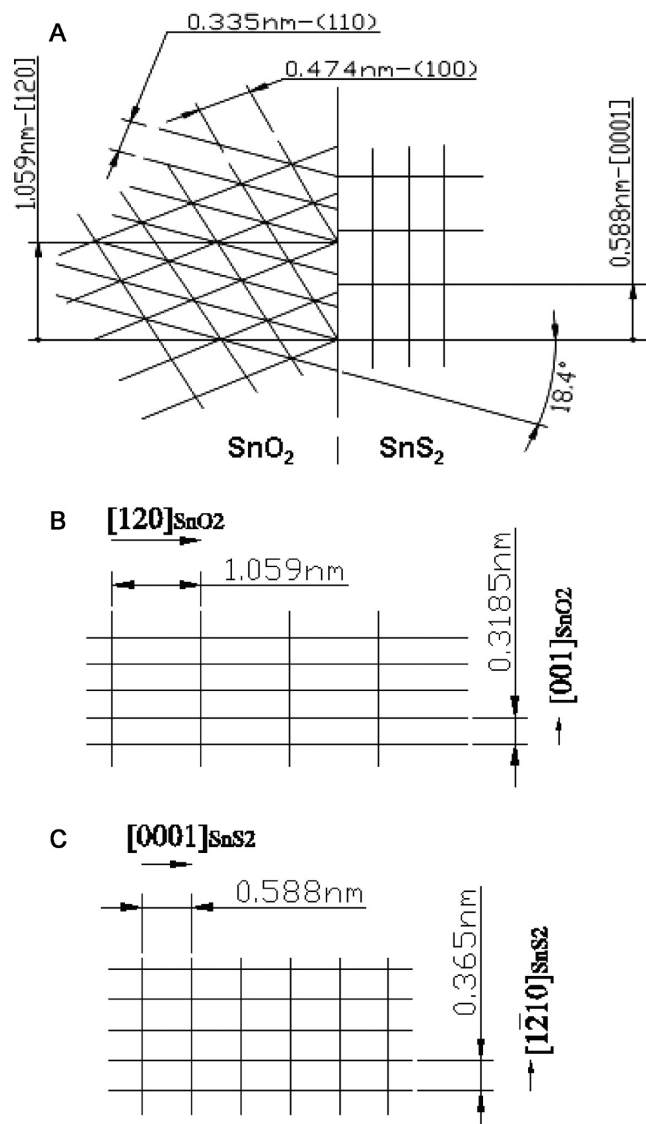on SnS$_2$ surface, because the energy of nucleation required in heterogeneous phase is generally lower than that in homogeneous phase.[39] Moreover, high surface energy of the emerging SnO$_2$ ultrafine nanoparticles also facilitates their combination with their precursor, the most adjacent SnS$_2$ nanoparticles. Thus, the selective oxidation of more reactive exposed crystal faces or surface defect centers of SnS$_2$ nanoparticles and in situ nucleation and growth/agglomeration of SnO$_2$ nanoparticles that produces the SnS$_2$/SnO$_2$ nanocomposites with a contact interface are more likely to occur, rather than the formation of a core–shell structure.

3.3. BET Surface Area. Figure 6 shows the N$_2$ adsorption/desorption isotherms of the as-prepared SnS$_2$, SnS$_2$/SnO$_2$-(a)–(d) and SnO$_2$. All the samples exhibited type IV isotherms with a hysteresis loop at relative pressure (P/P$_0$) between 0.4 and 1.0, indicating the presence of mesopores.[1,2,40] The formation of mesoporous structures can be ascribed to aggregation of the primary crystallites of the samples.[1,2,40] The values of the BET specific surface areas of the samples are listed in Table 1, which
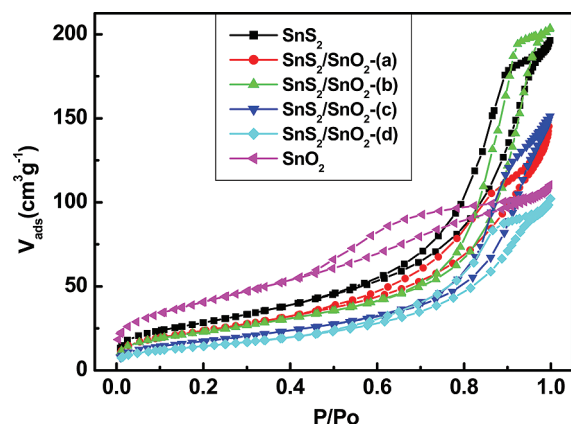
Figure 6. N_2 adsorption/desorption isotherms of the as-prepared SnS_2, SnS_2/SnO_2-(a)−(d), and SnO_2.
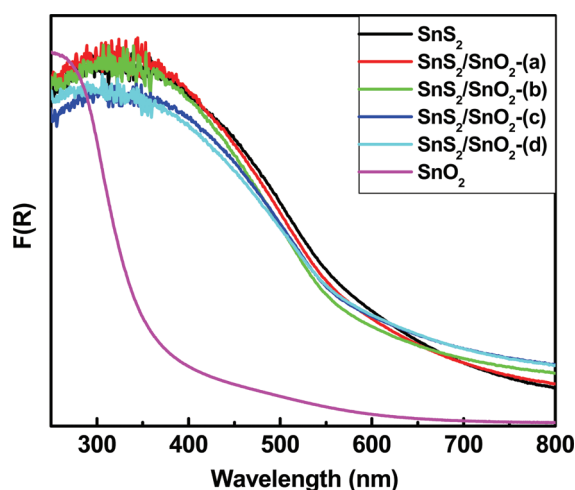

Figure 7. UV−vis diffuse reflectance spectra of SnS_2, SnS_2/SnO_2-(a)−(d) and SnO_2.

Figure 8. Plots of $(F(R)h\nu)^2$ vs $(h\nu)$ for estimation of the optical band gaps of SnS_2, SnS_2/SnO_2-(a)−(d), and SnO_2.

Figure 9. Photocatalytic decoloration of 20 mg/L MO aqueous solution over 0.3 g of SnS_2, SnS_2/SnO_2-(a)−(d), and SnO_2.

exhibit the following order: SnO_2 > SnS_2 > SnS_2/SnO_2-(a) > SnS_2/SnO_2-(b) > SnS_2/SnO_2-(c) > SnS_2/SnO_2-(d). As compared with single-phase SnO_2 or SnS_2 nanoparticles, the reduction in BET surface area of the SnS_2/SnO_2 nanocomposites should be another indication of the compacted agglomeration between their two components.

3.4. Optical Property. The UV−vis diffuse reflectance spectra of the as-prepared SnS_2, SnS_2/SnO_2-(a)−(d) and SnO_2 were measured and converted into the absorption spectra (Figure 7) using the Kubelka−Munk function (eqs 1 and 2)[41−45]

$$F(R_\infty) = (1 - R_\infty)^2/2R_\infty = \alpha/S \tag{1}$$

$$R_\infty = R_{sample}/R_{BaSO4} \tag{2}$$

where $F(R_\infty)$, R, α and S are the Kubelka−Munk function, reflectance, absorption coefficient and scattering coefficient, respectively. As can be seen from Figure 7, SnS_2 and $SnS_2/$ SnO_2-(a)−(d) displayed optical absorption capabilities nearly in the entire visible light spectrum, which is commonly defined in the wavelength range of 400−700 nm. The broad spectrum response implied that they may be good visible light-sensitive photocatalysts. According to a previous study,[9] the band gaps (E_g) of the as-prepared products were determined based on
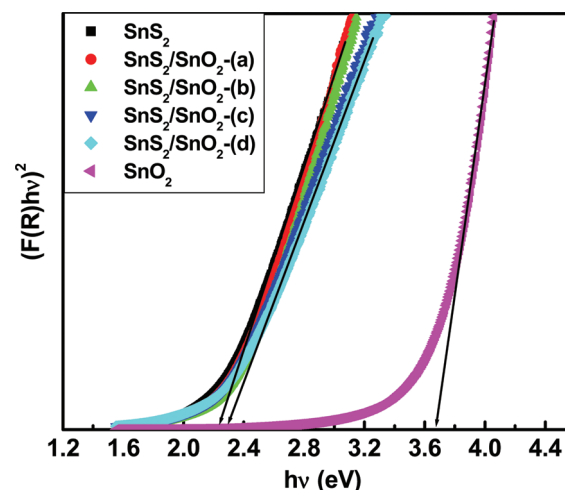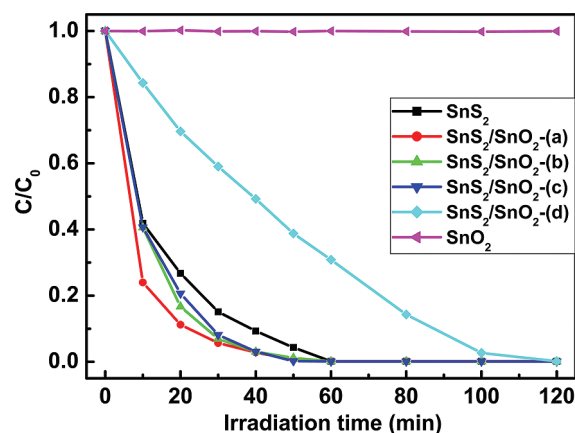
the theory of optical absorption for direct band gap semiconductors (eq 3)

$$\alpha h\nu = B(h\nu - E_g)^{1/2} \tag{3}$$

where $h\nu$ and B are discrete photon energy and a constant relative to the material, respectively. The value of α can be calculated from the diffuse reflectance data using the Kubelka−Munk function. But, for the diffused reflectance spectra, the Kubelka−Munk function can be used instead of α for estimating the optical absorption edge energy.[41−44] So, the curves of $(F(R)h\nu)^2$ vs $(h\nu)$ for the samples are plotted in Figure 8. By extrapolating the linear portion of the $(F(R)h\nu)^2$ vs $(h\nu)$ curves to $F(R) = 0$, the E_g values of SnS_2, SnS_2/SnO_2-(a)−(d), and SnO_2 were obtained and shown in Table 1.

3.5. Photocatalytic Tests. *3.5.1. Photocatalytic Activities of SnS_2, SnS_2/SnO_2-(a)−(d) and SnO_2.* Figure 9 shows the degradation of aqueous MO (20 mg/L) in the presence of 0.3 g of SnS_2, SnS_2/SnO_2-(a)−(d) and SnO_2 under visible light (λ > 420 nm) irradiation. C_0 and C are the concentrations of MO aqueous solution at the irradiation times of 0 (that is, after the dark adsorption equilibrium) and t min, respectively. As can be seen from Figure 9, the photocatalytic activities of the as-prepared
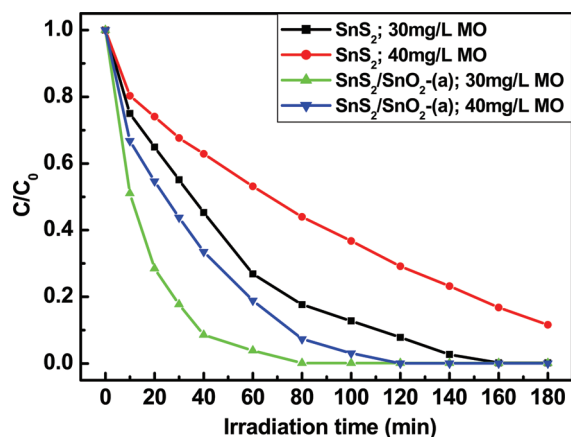
Figure 10. Photocatalytic decoloration of 30–40 mg/L MO aqueous solutions over 0.3 g of SnS₂ and SnS₂/SnO₂-(a).

Table 2. Calculated Values of Rate Constant (k) and Regression Coefficient (R) for All Sets of Photocatalytic Degradation Reactions

sample	amount of photocatalyst (g)	concentration of MO solution (mg/L)	$k \times 10^2$ (min^{-1})	R
SnS₂	0.3	20	5.941	0.9955
SnS₂	0.3	30	2.095	0.9986
SnS₂	0.3	40	0.968	0.9966
SnS₂	0.2	20	3.683	0.9962
SnS₂	0.1	20	1.750	0.9857
SnS₂/SnO₂-(a)	0.3	20	9.260	0.9890
SnS₂/SnO₂-(a)	0.3	30	5.966	0.9981
SnS₂/SnO₂-(a)	0.3	40	3.070	0.9904
SnS₂/SnO₂-(a)	0.2	20	7.311	0.9973
SnS₂/SnO₂-(a)	0.1	20	1.798	0.9951
SnS₂/SnO₂-(b)	0.3	20	8.818	0.9999
SnS₂/SnO₂-(c)	0.3	20	8.557	0.9984
SnS₂/SnO₂-(d)	0.3	20	1.938	0.9978
SnO₂	0.3	20	0	
PM-SnS₂/SnO₂	0.3	20	7.094	0.9899
PM-SnS₂/SnO₂	0.2	20	5.662	0.9971
PM-SnS₂/SnO₂	0.1	20	0.558	0.9993

SnS₂/SnO₂ nanocomposites depended on their SnO₂ contents. For example, the decolorization rates of MO over SnS₂/SnO₂-(a)–(c) were all faster than that over SnS₂, but an opposite result was obtained by comparison between SnS₂/SnO₂-(d) and SnS₂. Besides, no degradation of MO occurred in the presence of SnO₂ nanoparticles, indicating that SnO₂ nanoparticles alone had no photocatalytic activity under visible light ($\lambda > 420$ nm) irradiation. Considering that the dark adsorption amounts for MO followed the order of SnS₂ > SnS₂/SnO₂-(a) > SnS₂/SnO₂-(b) > SnS₂/SnO₂-(c) > SnS₂/SnO₂-(d) > SnO₂ (the C_0 values of MO solution for SnS₂, SnS₂/SnO₂-(a), SnS₂/SnO₂-(b), SnS₂/SnO₂-(c), SnS₂/SnO₂-(d), and SnO₂ were in turn, 8.0, 8.4, 13.6, 13.8, 16.0, and 19.0 mg/L), SnS₂/SnO₂-(a)–(c) should indeed have higher photocatalytic efficiencies than SnS₂ nanoparticles in terms of decolorizing more amounts of MO in shorter times.

As SnS₂ and SnS₂/SnO₂-(a) had similar dark adsorption capacities for MO, their photocatalytic activities were further compared by using higher concentrations of MO aqueous solutions. The obtained results are shown in Figure 10. Apparently, when the concentration of the MO aqueous solution was increased to 30–40 mg/L, SnS₂/SnO₂-(a) still displayed higher photocatalytic efficiencies than SnS₂ nanoparticles. Furthermore, the difference in their activities became even greater.

To quantitatively compare the photocatalytic activities of these samples, the reaction rate constants (k) were calculated by adopting the pseudofirst-order model as expressed by eq 4, which is generally used for photocatalytic degradation process if the initial concentration of pollutant is low[2,12,25–27,46–48]

$$\ln(C_0/C) = kt \qquad (4)$$

The plots of $\ln(C_0/C)$ versus irradiation time (t) for all sets of photocatalytic degradation reactions are provided in the Supporting Information (Figure S1). Table 2 shows the values of k and regression coefficient (R) derived from Figure S1 in the Supporting Information. It can be seen from Table 2 that the R values for most cases were close to 1, suggesting that the first order degradation kinetics can be used to explain the experimental results.[46] As expected, the k values in Table 2 agreed with the above analysis results of Figures 9 and 10.

3.5.2. Photocatalytic Action Mechanism. The valence band (VB) and conduction band (CB) potentials of semiconductors at the point of zero charge can be estimated by eq 5[10,12,25–27]

$$E_{VB} = X - E^e + 0.5E_g \qquad (5)$$

where E_{VB} is the VB potential, X is the electronegativity of the semiconductor which is the geometric mean of the electronegativity of the constituent atoms (it is worth noting that the electronegativity of an atom is the arithmetic mean of the atomic electron affinity and the first ionization energy), E^e is the energy of free electrons on the hydrogen scale (4.5 eV), and E_g is the band gap energy of the semiconductor. So far, considerable success had been achieved in predicting the relative band edge positions for many oxide and sulfide semiconductors using this method.[10,12,25–27] In our case, the calculated results were E_{CB}(SnS₂) = −0.135 eV, E_{VB}(SnS₂) = 2.115 eV and E_{CB}(SnO₂) = −0.08 eV, E_{VB}(SnO₂) = 3.58 eV. Although these data may not be the exact absolute values for the CB and VB potentials of SnS₂ and SnO₂, they should offer a correct estimation of the relative band edge positions of the two semiconductors. In addition, the present calculations were also consistent with the previous report by Xu et al.[33] Thus, a schematic diagram of the energy band structures of SnS₂/SnO₂ composite is illustrated in Figure 11, which is similar to that of the well studied CdS/TiO₂.[13–18]

When the SnS₂/SnO₂ nanocomposites were irradiated by visible light ($\lambda > 420$ nm), SnO₂ had no response ability due to its wide band gap ($E_g = 3.66$ eV), but the electrons in the VB of SnS₂ can be excited to its CB with simultaneous generation of the same amount of holes in its VB. The CB of SnO₂ was more positive than that of SnS₂, resulting in a local electric field.[13] As a result, the excited electrons can readily transfer from the CB of SnS₂ to the CB of SnO₂ via interface, whereas the generated holes still remained on the VB of SnS₂.[33] In this way, the photoinduced charge carriers in SnS₂ nanoparticles can be effectively separated, and accordingly their recombination was slowed down.[33] The efficient charge separation can increase the lifetime of the charge carriers and enhance the efficiency of the interfacial charge transfer to adsorbed substrates.[23] Moreover, SnO₂ nanoparticles can be sensitized via the aforementioned interfacial electron transfer process. So, it is reasonable that the SnS₂/SnO₂ nanocomposites
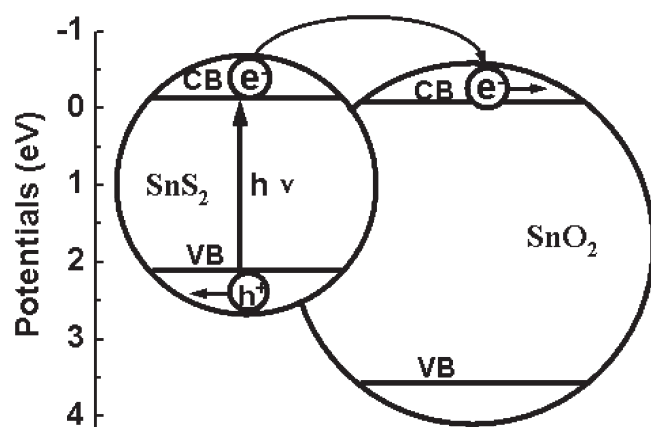
Figure 11. Diagram of the energy band structure and vectorial electron transfer in the SnS_2/SnO_2 composite semiconductors.
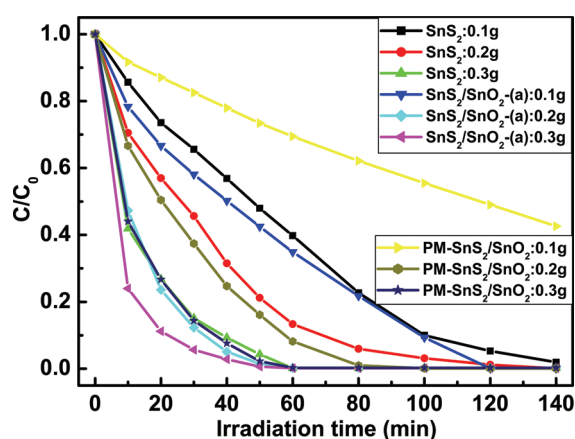
Figure 12. Comparison of the photocatalytic efficiencies of 0.1–0.3 g of SnS_2, SnS_2/SnO_2-(a) and PM-SnS_2/SnO_2.

with appropriate contents of SnO_2 (such as SnS_2/SnO_2-(a)–(c)) could demonstrate higher photocatalytic efficiencies than sole SnS_2 nanoparticles. On the other hand, the poorer photocatalytic activity of SnS_2/SnO_2-(d) may be interpreted from the following aspects. First, SnO_2 itself had no photocatalytic activity under visible light ($\lambda > 420$ nm) irradiation. The more mass ratio of SnO_2 meant the less mass ratio of the photocatalytic active SnS_2 in the nanocomposite, whose dose for each photocatalytic experiment was fixed at 0.3 g. The lower amounts of the photocatalytic active SnS_2 involved in the photocatalytic processes would bring about lower photocatalytic efficiencies, because the photocatalytic efficiencies of both SnS_2 nanoparticles and SnS_2/SnO_2 nanocomposites were directly proportional to their doses as shown later in Figure 12. Second, a large amount of SnO_2 and SnS_2 nanoparticles in SnS_2/SnO_2-(d) were not attached to each other (Figure 3e), which would undermine the interfacial electron transfer; or too much SnO_2 on SnS_2 surface possibly hindered the contact of SnS_2 with MO and blocked the visible light irradiation on SnS_2. Third, both the BET surface area and adsorption capacity for MO of SnS_2/SnO_2-(d) were smaller than those of SnS_2 nanoparticles and SnS_2/SnO_2-(a)–(c). Because the photocatalytic reactions are commonly believed to occur on the surface of the photocatalyst, the smaller BET surface area and less MO adsorption amount of

SnS_2/SnO_2-(d) may contribute to lower degradation rate of MO.[42,49–51]

3.5.3. Influence of Interface. To illustrate the influence and significance of the interface between composite semiconductors, the photocatalytic activities of 0.1–0.3 g of SnS_2, SnS_2/SnO_2-(a) and PM-SnS_2/SnO_2 were further compared. As can be seen from Figure 12 and Table 2, 0.1–0.3 g of SnS_2/SnO_2-(a) always demonstrated superior photocatalytic activity to the same amounts of SnS_2 and PM-SnS_2/SnO_2. Nevertheless, the comparison between SnS_2 nanoparticles and PM-SnS_2/SnO_2 gave a dose-dependent result: while 0.2–0.3 g of PM-SnS_2/SnO_2 showed higher photocatalytic efficiencies than the same amounts of SnS_2 nanoparticles, an opposite conclusion was drawn when their dose was decreased to 0.1 g. The foregoing results clearly indicated that the interface between SnS_2/SnO_2 composite nanoparticles played an important role in their photocatalytic activity. When a larger concentration (such as 0.2–0.3 g) of PM-SnS_2/SnO_2 was suspended in the MO aqueous solution with continuous magnetic stirring, there were still great chances for the nanoparticles of SnS_2 and SnO_2 to collide with each other to induce the instantaneous interface. Accordingly, the probability of photogenerated electron transfer and charge separation was also relatively high, making PM-SnS_2/SnO_2 have better photocatalytic activity than SnS_2 nanoparticles in the case of larger dose. Otherwise, when the concentration of PM-SnS_2/SnO_2 was too small, the chance of mutual collision between SnS_2 and SnO_2 nanoparticles and subsequent interfacial electron transfer became much less, plus SnO_2 itself had no photocatalytic activity under visible light irradiation, causing 0.1 g of PM-SnS_2/SnO_2 to have lower photocatalytic efficiency than the same amount of SnS_2 nanoparticles. Compared with that provided by the random collision between isolated SnS_2 and SnO_2 nanoparticles in PM-SnS_2/SnO_2, the tighter interface between closely attached SnS_2 and SnO_2 nanoparticles in SnS_2/SnO_2-(a) made the interfacial electron transfer more spatially available and smoother. Consequently, SnS_2/SnO_2-(a) performed the best under the aforementioned conditions of different doses of photocatalysts.

In addition, Figure 12 demonstrated that the dose of SnS_2/SnO_2-(a) played an important role in its photocatalytic efficiency. With an increase in the dose of SnS_2/SnO_2-(a), the degradation rate of MO was also enhanced. The enhancement in the degradation rate of MO with increased concentration of photocatalyst is a characteristic of heterogeneous catalysis, and can be rationalized in terms of the available active sites on the photocatalyst surface and the effective light penetration into the suspension.[52–54] But on the whole, it can be said that this kind of composite photocatalyst was highly efficient in degrading aqueous MO under visible light irradiation, for example, even the least dose (0.1 g) of SnS_2/SnO_2-(a) can achieve a complete decoloration of 300 mL of 20 mg/L MO solution within 120 min irradiation.

3.5.4. Photocatalytic Stability of SnS_2/SnO_2-(a). Because the stability of sulfide-based photocatalysts had always been a concern, it was important to investigate the stability and repeatability of the as-prepared SnS_2/SnO_2 nanocomposites in photocatalytic degradation of aqueous MO. So, in the present work, SnS_2/SnO_2-(a) was recycled eight times in the same photocatalytic reactions. After each cycle, which lasted for 60 min, the photocatalyst was separated from the suspension by filtration, washed with water and ethanol, dried in vacuum at 100 °C, and weighed for a new cycle. Taking into account the mass loss (mainly in the process of filtration) of photocatalyst during each cycle, the
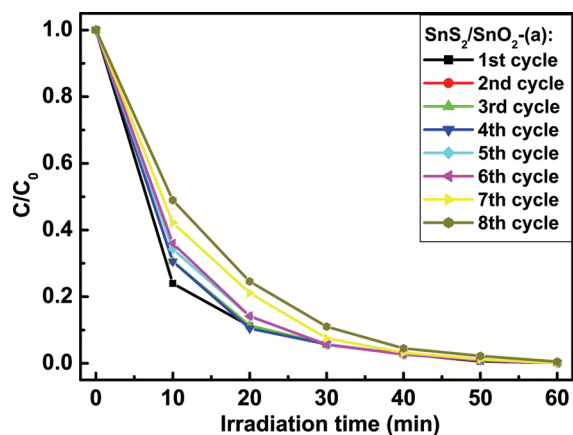
Figure 13. Photocatalytic performances of SnS_2/SnO_2-(a) in the reuse cycles.

seventh cycle must be conducted twice in order to accumulate enough sample for the eighth cycle, the sixth cycle must be conducted twice in order to accumulate enough sample for the seventh cycle, and so on. Figure 13 shows the photocatalytic performances of SnS_2/SnO_2-(a) in the first eight cycles. As can be seen, the photocatalytic activity of SnS_2/SnO_2-(a) deteriorated with the increase in the number of reuse cycles, but only very slightly. Even in the eighth cycle, the decoloration ratio of MO was still near 100% when subjected to visible light irradiation for 60 min. The above results suggested that SnS_2/SnO_2-(a) is a promising, efficient, and stable visible light-sensitive photocatalyst for the remediation of water polluted by chemically stable azo dyes, such as MO.

4. CONCLUSIONS

SnS_2/SnO_2 nanocomposites with adjustable contents of SnO_2 were synthesized via in situ hydrothermal oxidation of SnS_2 nanoparticles in different concentrations of H_2O_2 aqueous solutions at 180 °C for 0−12 h. This method is simple, cost-effective, and capable of preparing SnS_2/SnO_2 nanocomposites with a tighter interface.

Through the photocatalytic experiments using aqueous MO as a target contaminant under visible light ($\lambda > 420$ nm) irradiation, the following results were obtained: (1) the photocatalytic activities of SnS_2/SnO_2 nanocomposites depended on their SnO_2 contents; (2) 0.1−0.3 g of SnS_2/SnO_2-(a) always demonstrated higher photocatalytic efficiencies than the same amounts of SnS_2 nanoparticles and PM-SnS_2/SnO_2 in decolorizing 20−40 mg/L MO aqueous solutions; (3) SnS_2/SnO_2-(a) had good photocatalytic stability, which showed little loss in activity during the eight reuse cycles. It is believed that the tight interface between closely attached SnS_2 and SnO_2 nanoparticles played an important role in the superior photocatalytic performance of SnS_2/SnO_2-(a).

ASSOCIATED CONTENT

S **Supporting Information.** Plots of $\ln(C_0/C)$ versus irradiation time (t) for all sets of photocatalytic degradation reactions. This material is available free of charge via the Internet at http://pubs.acs.org.

AUTHOR INFORMATION

Corresponding Author
*Tel: 086 0514 87962581. Fax: 086 0514 87975244. E-mail: zhangyc@yzu.edu.cn.

ACKNOWLEDGMENT

REFERENCES

(1) Araujo, P. Z.; Luca, V.; Bozzano, P. B.; Bianchi, H. L.; Soler-Illia, G. J. A. A.; Blesa, M. A. *ACS Appl. Mater. Interfaces* **2010**, *2*, 1663–1673.
(2) Feng, Y.; Li, L.; Ge, M.; Guo, C.; Wang, J.; Liu, L. *ACS Appl. Mater. Interfaces* **2010**, *2*, 3134–3140.
(3) Lü, X.; Huang, F.; Wu, J.; Ding, S.; Xu, F. *ACS Appl. Mater. Interfaces* **2011**, *3*, 566–572.
(4) Rehman, S.; Ullah, R.; Butt, A. M.; Gohar, N. D. *J. Hazard. Mater.* **2009**, *170*, 560–569.
(5) Xiong, S.; Xi, B.; Qian, Y. *J. Phys. Chem. C* **2010**, *114*, 14029–14035.
(6) Wang, C.; Ao, Y.; Wang, P.; Hou, J.; Qian, J.; Zhang, S. *Mater. Lett.* **2010**, *64*, 439–441.
(7) Guo, Y.; Wang, L.; Yang, L.; Zhang, J.; Jiang, L.; Ma, X. *Mater. Lett.* **2011**, *65*, 486–489.
(8) Lei, Y.; Song, S.; Fan, W.; Xing, Y.; Zhang, H. *J. Phys. Chem. C* **2009**, *113*, 1280–1285.
(9) Zhang, Y. C.; Du, Z. N.; Li, S. Y.; Zhang, M. *Appl. Catal., B* **2010**, *95*, 153–159.
(10) Yang, C.; Wang, W.; Shan, Z.; Huang, F. *J. Solid State Chem.* **2009**, *182*, 807–812.
(11) He, H. Y.; Huang, J. F.; Cao, L. Y.; Wu, J. P.; He, Z.; Luo, L. *J. Optoelectron. Adv. Mater.* **2007**, *9*, 3781–3784.
(12) Gao, C.; Li, J.; Shan, Z.; Huang, F.; Shen, H. *Mater. Chem. Phys.* **2010**, *122*, 183–187.
(13) Xie, Y.; Ali, G.; Yoo, S. H.; Cho, S. O. *ACS Appl. Mater. Interfaces* **2010**, *2*, 2910–2914.
(14) Zyoud, A. H.; Zaatar, N.; Saadeddin, I.; Ali, C.; Park, D.; Campet, G.; Hilal, H. S. *J. Hazard. Mater.* **2010**, *173*, 318–325.
(15) Yan, X.; Liu, G.; Wang, L.; Wang, Y.; Zhu, X.; Zou, J.; Lu, G. Q. M. *J. Mater. Res.* **2010**, *25*, 182–188.
(16) Li, G. S.; Zhang, D. Q.; Yu, J. C. *Environ. Sci. Technol.* **2009**, *43*, 7079–7085.
(17) Banerjee, S.; Mohapatra, S. K.; Das, P. P.; Misra, M. *Chem. Mater.* **2008**, *20*, 6784–6791.
(18) Wu, L.; Yu, J. C.; Fu, X. *J. Mol. Catal. A.: Chem.* **2006**, *244*, 25–32.
(19) Kang, K.; Liu, S.; Yang, L.; Cai, Q.; Grimes, C. A. *ACS Appl. Mater. Interfaces* **2011**, *3*, 746–749.
(20) Wang, R.; Xu, D.; Liu, J. B.; Li, K. W.; Wang, H. *Chem. Eng. J.* **2011**, *168*, 455–460.
(21) Zhou, W.; Liu, H.; Wang, J.; Liu, D.; Du, J.; Cui, J. *ACS Appl. Mater. Interfaces* **2010**, *2*, 2385–2392.
(22) Zhang, J.; Zhu, H.; Zheng, S.; Pan, F.; Wang, T. *ACS Appl. Mater. Interfaces* **2009**, *1*, 2111–2114.
(23) Zhang, Z.; Shao, C.; Li, X.; Wang, C.; Zhang, M.; Liu, Y. *ACS Appl. Mater. Interfaces* **2010**, *2*, 2915–2923.
(24) Leghari, S. A. K.; Sajjad, S.; Chen, F.; Zhang, J. *Chem. Eng. J.* **2011**, *166*, 906–915.
(25) Zhang, X.; Zhang, L.; Xie, T.; Wang, D. *J. Phys. Chem. C* **2009**, *113*, 7371–7378.
(26) Lin, X.; Xing, J.; Wang, W.; Shan, Z.; Xu, F.; Huang, F. *J. Phys. Chem. C* **2007**, *111*, 18288.

(27) Lin, X.; Huang, F.; Xing, J.; Wang, W.; Xu, F. *Acta Mater.* **2008**, *56*, 2699–2705.

(28) Li, G.; Gray, K. A. *Chem. Phys.* **2007**, *339*, 173–187.

(29) Huang, H.; Li, D.; Lin, Q.; Zhang, W.; Shao, Y.; Chen, Y.; Sun, M.; Fu, X. *Environ. Sci. Technol.* **2009**, *43*, 4164–4168.

(30) Cao, T.; Li, Y.; Wang, C.; Shao, C.; Liu, Y. *Langmuir* **2011**, *27*, 2946–2952.

(31) Wang, C.; Shao, C.; Zhang, X.; Liu, Y. *Inorg. Chem.* **2009**, *48*, 7261–7268.

(32) Zhang, Z.; Shao, C.; Li, X.; Zhang, L.; Xue, H.; Wang, C.; Liu, Y. *J. Phys. Chem. C* **2010**, *114*, 7920–7925.

(33) Xu, B.; Cheng, H. M.; Wang, Y. Q.; Ma, J. M. *Chem. J. Chin. Univ.* **1999**, *20*, 997–1001.

(34) Moulder, J. F.; Stickle, W. F.; Sobol, P. E.; Bomben, K. D. In *Handbook of X-ray Photoelectron Spectroscopy*; Chastain, J., Ed.; Perkin-Elmer Corp.: New York, 1992.

(35) Seo, J.; Jang, J.; Park, S.; Kim, C.; Park, B.; Cheon, J. *Adv. Mater.* **2008**, *20*, 4269–4273.

(36) Duhalde, S.; Arcondo, B.; Sirkin, H. *Hyperfine Interact.* **1991**, *66*, 287–294.

(37) Sun, C. Q. *Prog. Solid State Chem.* **2007**, *35*, 1–159.

(38) Shim, M.; McDaniel, H. *Curr. Opin. Solid State Mater. Sci.* **2010**, *14*, 83–94.

(39) Carbone, L.; Cozzoli, P. D. *Nano Today* **2010**, *5*, 449–493.

(40) Raj, K. J. A.; Viswanathan, B. *ACS Appl. Mater. Interfaces* **2009**, *1*, 2462–2469.

(41) Wodka, D.; Bielańska, E.; Socha, R. P.; Wodka, M. E.; Gurgul, J.; Nowak, P.; Warszyński, P.; Kumakiri, I. *ACS Appl. Mater. Interfaces* **2010**, *2*, 1945–1953.

(42) Mejía, M. I.; Marín, J. M.; Restrepo, G.; Pulgarín, C.; Mielczarski, E.; Mielczarski, J.; Stolitchnov, I.; Kiwi, J. *ACS Appl. Mater. Interfaces* **2009**, *1*, 2190–2198.

(43) Zhang, L.; Cao, X. F.; Chen, X. T.; Xue, Z. L. *J. Colloid Interface Sci.* **2011**, *354*, 630–636.

(44) Dong, H.; Li, Z.; Xu, X.; Ding, Z.; Wu, L.; Wang, X.; Fu, X. *Appl. Catal. B: Environ.* **2009**, *89*, 551–556.

(45) Dong, W.; Lee, C. W.; Lu, X.; Sun, Y.; Hua, W.; Zhuang, J.; Zhang, S.; Chen, J.; Hou, H.; Zhao, D. *Appl. Catal., B* **2010**, *95*, 197–207.

(46) Priya, D. N.; Modak, J. M.; Raichur, A. M. *ACS Appl. Mater. Interfaces* **2009**, *1*, 2684–2693.

(47) Mahanta, D.; Manna, U.; Madras, G.; Patil, S. *ACS Appl. Mater. Interfaces* **2011**, *3*, 84–92.

(48) Mu, J.; Shao, C.; Guo, Z.; Zhang, Z.; Zhang, M.; Zhang, P.; Chen, B.; Liu, Y. *ACS Appl. Mater. Interfaces* **2011**, *3*, 590–596.

(49) Rajeshwar, K.; Osugi, M. E.; Chanmanee, W.; Chenthamarakshan, C. R.; Zanoni, M. V. B.; Kajitvichyanukul, P.; Krishnan-Ayer, R. *J. Photochem. Photobiol. C: Photochem. Rev.* **2008**, *9*, 171–192.

(50) Ji, P.; Zhang, J.; Chen, F.; Anpo, M. *Appl. Catal., B* **2009**, *85*, 148–154.

(51) Zheng, L.; Zheng, Y.; Chen, C.; Zhan, Y.; Lin, X.; Zheng, Q.; Wei, K.; Zhu, J. *Inorg. Chem.* **2009**, *48*, 1819–1825.

(52) Rauf, M. A.; Ashraf, S. S. *Chem. Eng. J.* **2009**, *151*, 10–18.

(53) Konstantinou, I. K.; Albanis, T. A. *Appl. Catal., B* **2004**, *49*, 1–14.

(54) Akpan, U. G.; Hameed, B. H. *J. Hazard. Mater.* **2009**, *170*, 520–529.